RESEARCH ARTICLE

WILEY

Stabilizing layered superlattice MoSe$_2$ anodes by the rational solvation structure design for low-temperature aqueous zinc-ion batteries

Zeheng Lv[1] | Yuanhong Kang[1] | Rong Tang[1] | Jin Yang[1] | Guanhong Chen[1] |
Yuhan Hu[1,2] | Pengxiang Lin[1] | Huiya Yang[1] | Qilong Wu[1] | Minghao Zhang[1] |
Fenghua Chen[2] | Yueying Peng[3] | Yang Yang[1] (ORCID) | Jinbao Zhao[1]

[1]State Key Laboratory of Physical Chemistry of Solid Surfaces, State-Province Joint Engineering Laboratory of Power Source Technology for New Energy Vehicle, Tan Kah Kee Innovation Laboratory (IKKEM), College of Chemistry and Chemical Engineering, Xiamen University, Xiamen, China

[2]School of Resources and Chemical Engineering, Sanming University, Sanming, China

[3]International Center for Young Scientists, Center for Green Research on Energy and Environmental Materials, National Institute for Material Science, Tsukuba, Ibaraki, Japan

Correspondence
Yang Yang and Jinbao Zhao.
Email: yangyang419@xmu.edu.cn and jbzhao@xmu.edu.cn

Abstract

Aqueous zinc-ion batteries (AZIBs) have attracted widespread attention due to their intrinsic merits of low cost and high safety. However, the poor thermodynamic stability of Zn metal in aqueous electrolytes inevitably cause Zn dendrites growth and interface parasitic side reactions, resulting in unsatisfactory cycling stability and low Zn utilization. Replacing Zn anode with intercalation-type anodes have emerged as a promising alternative strategy to overcome the above issues but the lack of appropriate anode materials is becoming the bottleneck. Herein, the interlayer structure of MoSe$_2$ anode is preintercalated with long-chain polyvinyl pyrrolidone (PVP), constructing a periodically stacked p-MoSe$_2$ superlattice to activate the reversible Zn^{2+} storage performance (203 mAh g^{-1} at 0.2 A g^{-1}). To further improve the stability of the superlattice structure during cycling, the electrolyte is also rationally designed by adding 1,4-Butyrolactone (γ-GBL) additive into 3 M Zn(CF$_3$SO$_3$)$_2$, in which γ-GBL replaces the H$_2$O in Zn^{2+} solvation sheath. The preferential solvation of γ-GBL with Zn^{2+} effectively reduces the water activity and helps to achieve an ultra-long lifespan of 12,000 cycles for p-MoSe$_2$. More importantly, the reconstructed solvation structure enables the operation of p-MoSe$_2$|| Zn$_x$NVPF (Na$_3$V$_2$(PO$_4$)$_2$O$_2$F) AZIBs at an ultra-low temperature of −40°C, which is expected to promote the practical applications of AZIBs.

KEYWORDS
intercalation-type anodes, p-MoSe$_2$||Zn$_x$NVPF, periodically stacked p-MoSe$_2$ superlattice, solvation sheath, ultra-long lifespan

1 | INTRODUCTION

The emerging environment-friendly, low-cost, and high-safety Zn-ion batteries (ZIBs) based on high-ion-conductivity aqueous electrolytes receive great research enthusiasm due to high theoretical capacity (820 mAh g^{-1}) and relatively low redox potential (−0.763 V vs. standard hydrogen electrode) of Zn^{2+}/Zn.[1] Although the Mn-O, V-O, organic materials, and Prussian blue analogs are demonstrated as available

cathodes for accommodating Zn^{2+} ions in ZIBs,[2-4] the thermodynamically unstable Zn metal anode in an aqueous electrolyte faces severe problems of Zn dendrite growth and interfacial hydrogen evolution reaction (HER), which push researchers to develop advanced strategies to prevent these side reactions.[5-11] However, the inherent competitive reaction between Zn^{2+} deposition and HER causes the inevitable interface parasitic side reactions and irreversible loss of a certain amount of Zn^{2+} ions.

To solve these issues fundamentally, it is ingenious to replace Zn metal with intercalation-type anode. There are irreplaceable advantages that can be summarized as follows: (1) The thermodynamic compatibility between intercalation-type anode and aqueous electrolyte could be adjusted not only through changing the contact interface characteristic but also via optimizing the crystalline structure of anode material. (2) The relatively higher Zn^{2+} intercalation-voltage could effectively inhibit the HER reaction, so that the localized pH at the electrode/electrolyte interface could be stabilized and the growth of hydroxide sulfate zinc (dead Zn) would be suppressed. Therefore, the Coulombic efficiency, Zn^{2+} utilization, and cycling stability of aqueous zinc-ion batteries (AZIBs) should be improved after replacing Zn metal with intercalation-type anode.

Nevertheless, the significant electrostatic interaction between divalent Zn^{2+} and the structural framework of anode material will restrict Zn^{2+} ions' diffusion and intercalation. Actually, the raw electrode materials must experience effective modification before processing into electrodes. Except for the defect introduction and interlayer-space expansion,[12-15] the emerging superlattice electrode design is an effective way to exploit the reversible Zn^{2+} storage capability of intercalation-type anode. Generally, as a two-dimensional (2D) superstructure, the superlattice is formed by soft organic long-chain molecules and rigid inorganic hosts.[16-18] In addition, the inorganic monolayer is separated by organic layers alternately in a superlattice structure, which causes the generation of 2D vertically stacked organic–inorganic periodical architecture. The enlarged interlayer space of superlattice breaks the pristine structural limitation of 2D intercalation-type electrode, contributing to the smooth hydration Zn^{2+} ions transport and moderate inherent electrostatic interaction. Moreover, the structural stability of superlattice can be improved because the pillar effect turns severe volume changes during divalent Zn^{2+} ion intercalation/de-intercalation processes into more controllable ones. For instance, after preintercalation of cetyl-trimethylammonium bromide (CTAB), the MoS_2-CTAB superlattice shows high-rate performance over 2000 cycles at 10 A g^{-1}[16] and the periodically stacked CuS-CTAB superlattice can even stand over 3000

cycles.[17] However, the cycling stability of the super-lattice structure will deteriorate inevitably because of the continuous insertion of active water molecules along with rapid Zn^{2+} intercalation. Thus, it is necessary to regulate the solvation structure of Zn^{2+} in electrolyte so that the long-term cycling performance of superlattice anode can be achieved for AZIBs.

In this work, the long-chain polyvinyl pyrrolidone (PVP) is preintercalated into layer $MoSe_2$ via a one-step solvothermal reaction, resulting in the successful formation of a periodically stacked p-$MoSe_2$ superlattice at the first time (Figure 1A). Unexpectedly, p-$MoSe_2$ delivers 202.3 mAh g^{-1} at 0.2 A g^{-1}, while $MoSe_2$ without superlattice displays an almost negligible capacity of 16.3 mAh g^{-1}, firmly verifying the excellent structural advantage of superstructure. Furthermore, the 1,4-Butyrolactone (γ-GBL) additive is added into 3 M $Zn(CF_3SO_3)_2$ to reduce the water activity. Finally, the cooperative manipulation of the superlattice structure and solvation shell enables p-$MoSe_2$ electrode to show a stable long-term cycling of 12,000 cycles at 2 A g^{-1}. Encouragingly, the high-energy p-$MoSe_2$‖ZnI_2 and long-term stable p-$MoSe_2$‖ Zn_xNVPF rocking chair ZIBs are also fabricated successfully, and p-$MoSe_2$‖Zn_xNVPF full battery even displays 38.7 mAh g^{-1} within 320 cycles at −40°C.

2 | RESULTS AND DISCUSSION

The p-$MoSe_2$ superlattice with a nano-flower morphology is synthesized after inserting organic long-chain PVP molecules into the interlayer structure of $MoSe_2$ (Figure 1A and Figure S1) and the pure $MoSe_2$ also possesses the same morphology with the similar synthetic route (Figure S2). To examine the superstructural characteristic, the X-ray diffraction (XRD) was adopted firstly. The XRD results reveal that there are three diffraction peaks located at 4.02°, 8.16°, and 12.72°, respectively, with ploid relationship (Figure 1B), possibly corresponding to the (002), (004), and (006) peaks of p-$MoSe_2$ superlattice.[18] When compared with $MoSe_2$, p-$MoSe_2$ is also equipped with the structural feature of 2H $MoSe_2$ (JCPDS No. 29–0914) (Figure 1C). The characteristic C-N (1660 cm^{-1}) and C=O (1286 cm^{-1}) peaks in Fourier transform infrared (FTIR) spectra (Figure S3), sharp D/G peaks in Raman spectra (Figure S4), obvious N 1s signal in X-ray photoelectron spectroscopy (XPS) spectra (Figure S5), and the even distribution of Mo, Se, O, N, and C (Figure S1) in p-$MoSe_2$ imply that the periodically stacked superlattice layer $MoSe_2$ (p-$MoSe_2$) is formed firmly. In addition, it is worth noting that the interlayer distance of p-$MoSe_2$ is enlarged from ≈6.5 Å ($MoSe_2$) to ≈22.1 Å according to Bragg's equation (Figure 1G and Figure S6). Generally, the interlayer van der Waals force of layered transition metal dichalcogenide is related to
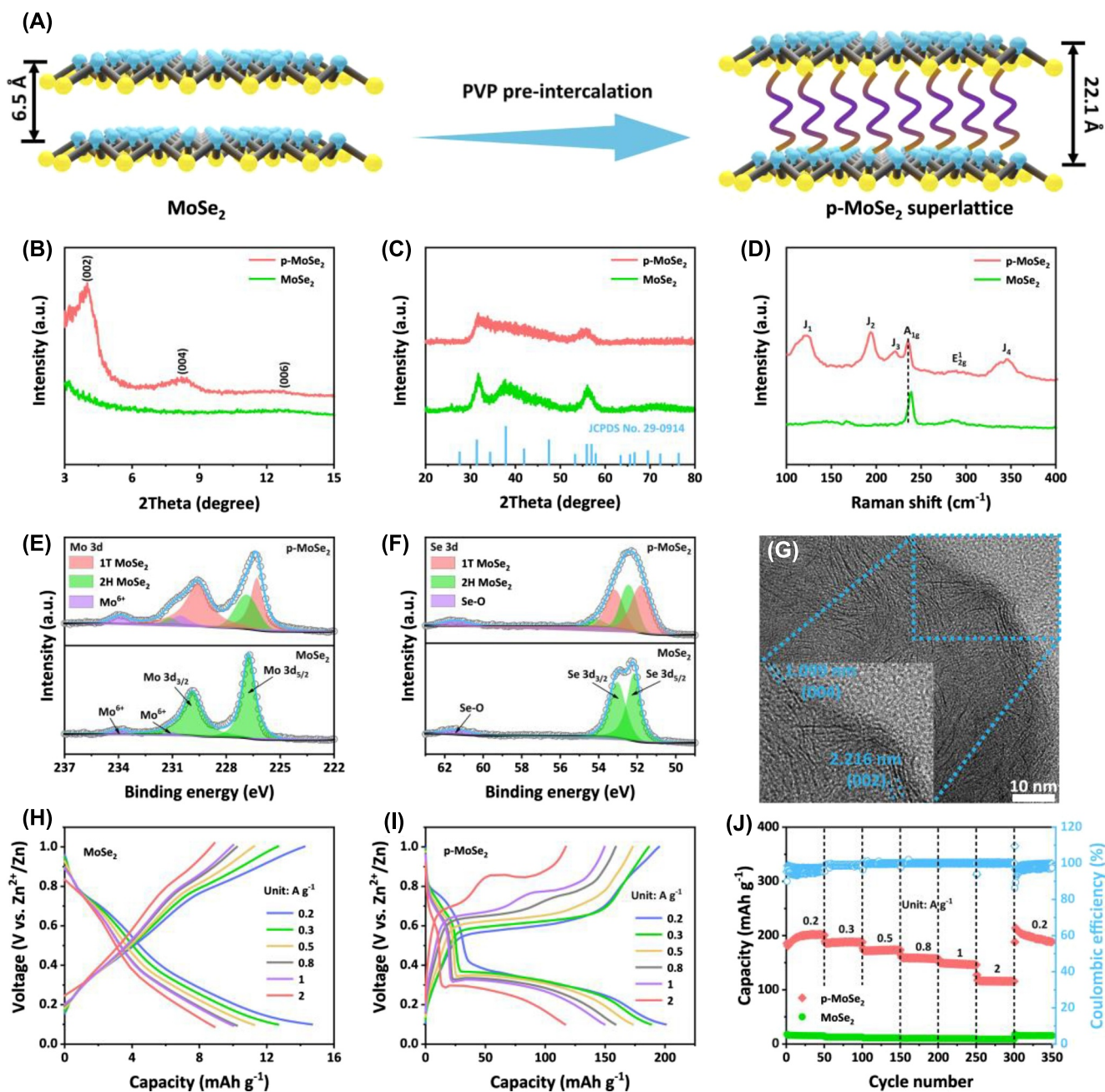
FIGURE 1 (A) Schematic of the formation of p-MoSe$_2$ superlattice. X-ray diffraction patterns of (B) 3°–15° and (C) 20°–80° for MoSe$_2$ and p-MoSe$_2$. (D) Raman spectra of MoSe$_2$ and p-MoSe$_2$. (E) Mo 3d and (F) Se 3d X-ray photoelectron spectroscopy spectra of MoSe$_2$ and p-MoSe$_2$. (G) Transmission electron microscope image of p-MoSe$_2$. Charge–discharge profiles of (H) MoSe$_2$ and (I) p-MoSe$_2$ at different current densities. (J) Rate performance of MoSe$_2$ and p-MoSe$_2$.

the interlayer distance.[15,19] In Figure 1D, both MoSe$_2$ and p-MoSe$_2$ display basic in-plane (E_{2g}^1) and out-of-plane (A_{1g}) vibration signals of hexagonal 2H phase in Raman spectra. The red shift of A_{1g} peak indicates the weakened van der Waals interaction force in the interlayer structure of p-MoSe$_2$.[20,21] Typically, a single MoSe$_2$ layer is sandwiching an Mo plane between two Se atomic planes and the different layer stacking mode is bound to shape various crystalline structures including stable hexagonal 2H and/or meta-stable

trigonal 1T phases.[21] Thus, the metallic 1T (J$_1$, J$_2$, J$_3$, and J$_4$ peaks) and 2H phases occur in highly ordered periodically stacked p-MoSe$_2$ superlattice simultaneously, while there is only one 2H phase in MoSe$_2$. The hybrid phases were also measured by X-ray photoelectron spectroscopy (XPS). In Figure 1E, only a single 2H phase in pure MoSe$_2$, and the peaks of Mo 3d$_{3/2}$ and Mo 3d$_{5/2}$ at 229.9 and 226.8 eV can be assigned to Mo^{4+}, respectively.[21,22] Different from pure MoSe$_2$, the Mo 3d spectra with a distinctive shape for p-MoSe$_2$ could be

clearly split into 1T and 2H phases. The Se 3d spectra of p-MoSe$_2$ also can be transformed into hybrid phases quantitatively in Figure 1F.[23] Combined with the Mo 3d and Se 3d spectra in XPS, it can be found that the higher content of the metallic 1T phase dominate the hybrid phases of p-MoSe$_2$ such that the electronic conductivity of p-MoSe$_2$ could be enhanced. In addition, a little content of Mo^{6+} and Se-O species for MoSe$_2$ and p-MoSe$_2$ could be attributed to the surface oxide reaction rationally.[24]

With weak interlayer interaction and improved electronic conductivity, the hybrid-phase p-MoSe$_2$ superlattice can exhibit appreciable capability of accommodating a large amount of Zn^{2+} ions with a fast rate. As shown in Figure 1H–J, the discharge–charge profiles of p-MoSe$_2$ are strikingly different from that of MoSe$_2$. Instead of the nearly linear charge–discharge curves of MoSe$_2$, the flat discharge and charge plateaus of p-MoSe$_2$ electrode appear at around 0.3–0.4 V and 0.5–0.6 V, respectively, demonstrating that the large enough interlayer space of superlattice favors more Zn^{2+} ions to intercalate into the bulk of p-MoSe$_2$ electrode. The high capacities of 202.3, 187.9, 173.7, 158.9, 148.6, and 116.3 mAh g^{-1} are delivered by p-MoSe$_2$ electrode at 0.2, 0.3, 0.5, 0.8, 1, and 2 A g^{-1}, respectively, while the pure MoSe$_2$ exhibits negligible capacities of 16.3, 12.8, 11.3, 10.4, 10.0, and 8.9 mAh g^{-1} at the same current densities. After 300 cycles, both MoSe$_2$ and p-MoSe$_2$ show higher capacity while compared with the initial state at 0.2 A g^{-1}, which can be ascribed to the activation process during repeated cycling performance.[15]

According to the above rate performance of p-MoSe$_2$, it can be estimated that only 57.5% of the capacity at 0.2 A g^{-1} can be retained at 2 A g^{-1}, meaning that the high-rate performance of p-MoSe$_2$ superlattice needs to be further improved. This unsatisfied retention at a high rate may be attributed to the sophisticated interfacial charge transfer process determined by the solvation structure of hydration Zn^{2+} ions in electrolytes.[25–28] Therefore, the high-rate cycling performance probably could be realized through regulating the solvation shell of Zn^{2+} ions after adding the effective additives into 3 M Zn(CF$_3$SO$_3$)$_2$.[25]

In 3 M Zn(CF$_3$SO$_3$)$_2$, a Zn^{2+} ion coordinates with six H$_2$O molecules in the inner solvation shell (Figure 2G, Type I), two CF$_3$SO$_3^-$ (OTF$^-$) anions and other H$_2$O molecules cointeract with Zn^{2+} ion symmetrically in the outer shell.[29] Recently, Li's group demonstrated that Zn^{2+} ion prefers to coordinate with γ-GBL additives instead of H$_2$O molecules in 2 M ZnSO$_4$ aqueous electrolyte,[25] thereby breaking the pristine solvation structure of Zn[(H$_2$O)$_6$]$^{2+}$ and forming a new solvation sheath including the participation of γ-GBL. In this work, γ-GBL also serves as an additive to regulate the chemical coordination

environment of Zn[(H$_2$O)$_6$]$^{2+}$ in 3 M Zn(CF$_3$SO$_3$)$_2$ (Zn(OTF)$_2$). In Figure 2C, the characteristic peak of C=O stretching vibration derived from γ-GBL shifts to a lower wavenumber in γ-Zn due to the strong interaction between Zn^{2+} and γ-GBL solvent,[25] but there is no obvious change of $^-$SO$_3$ vibration peak in both 3 M Zn(OTF)$_2$ and γ-Zn can be observed in FTIR spectra. For Raman spectra in Figure 2F, both $^-$SO$_3$ and C-C stretching vibration peaks of γ-Zn shift to a higher wavenumber, reflecting the enhanced binding force between Zn^{2+} and $^-$SO$_3$/C-C.[25,29,30] Hence, it can be hypothesized that γ-GBL may participate in the first (inner) Zn^{2+} solvation shell because the lone pair electrons of carbonyl oxygen can promote γ-GBL to interact with Zn^{2+} strongly. Naturally, with the steric hindrance effect, the coordination between active water molecules and Zn^{2+} ions may be weakened due to the existence of the relatively large γ-GBL molecules in the inner Zn^{2+} solvation shell and then the electrostatic interaction of OTF$^-$ and Zn^{2+} tend to strengthen subsequently.

To verify this conjecture, molecular dynamic (MD) simulations were conducted to investigate the solvation structures of Zn^{2+} in 3 M Zn(OTF)$_2$ and γ-Zn. As expected, per Zn^{2+} ion tends to coordinate with around five but not six solvated water molecules (Figure 2D) after introducing 30 vol% γ-GBL in cosolvent electrolyte named γ-Zn (Figure 2E). In addition, the significant interaction between Zn^{2+} and γ-GBL may provide evidence that the Type II solvation structure dominates the coordination environment in γ-Zn. Meanwhile, it is worth noting that a little part of OTF$^-$ anions would also participate to coordinate with Zn^{2+} in the primary solvation shell (Type III). Based on such a regulated Zn^{2+} solvation structure with decreased amount of water molecules and stronger binding force between Zn^{2+} and γ-GBL, it is rationally believed that the interfacial desolvation kinetics and the high-rate performance of p-MoSe$_2$ could be improved.

To analyze the redox mechanism of p-MoSe$_2$ electrode in γ-Zn, cyclic voltammetry (CV) test was performed at 0.1 mV s^{-1} in Figure 3A. From 0.1 to 1 V (vs. Zn^{2+}/Zn), the response current in γ-Zn is higher than that in 3 M Zn(OTF)$_2$, indicating the reconstructed solvated Zn^{2+} ions in γ-Zn can intercalate into p-MoSe$_2$ more easily. For the whole intercalation/deintercalation processes, there is only a pair of redox that peaks at 0.34 (cathodic) and 0.68 V (anodic) for p-MoSe$_2$ in γ-Zn, respectively, but there are two cathodic peaks in 3 M Zn(OTF)$_2$ at around 0.35 and 0.25 V, respectively, and two corresponded anodic peaks located at 0.55 and 0.67 V, respectively. Such a distinctive CV result in γ-Zn can be reflected in the typical discharge–charge curves at 0.2 A g^{-1}. In Figure 3B, p-MoSe$_2$ exhibits a faster voltage decline above 0.4 V in γ-Zn, and then the subsequent capacity is more concentrate at the voltage region between
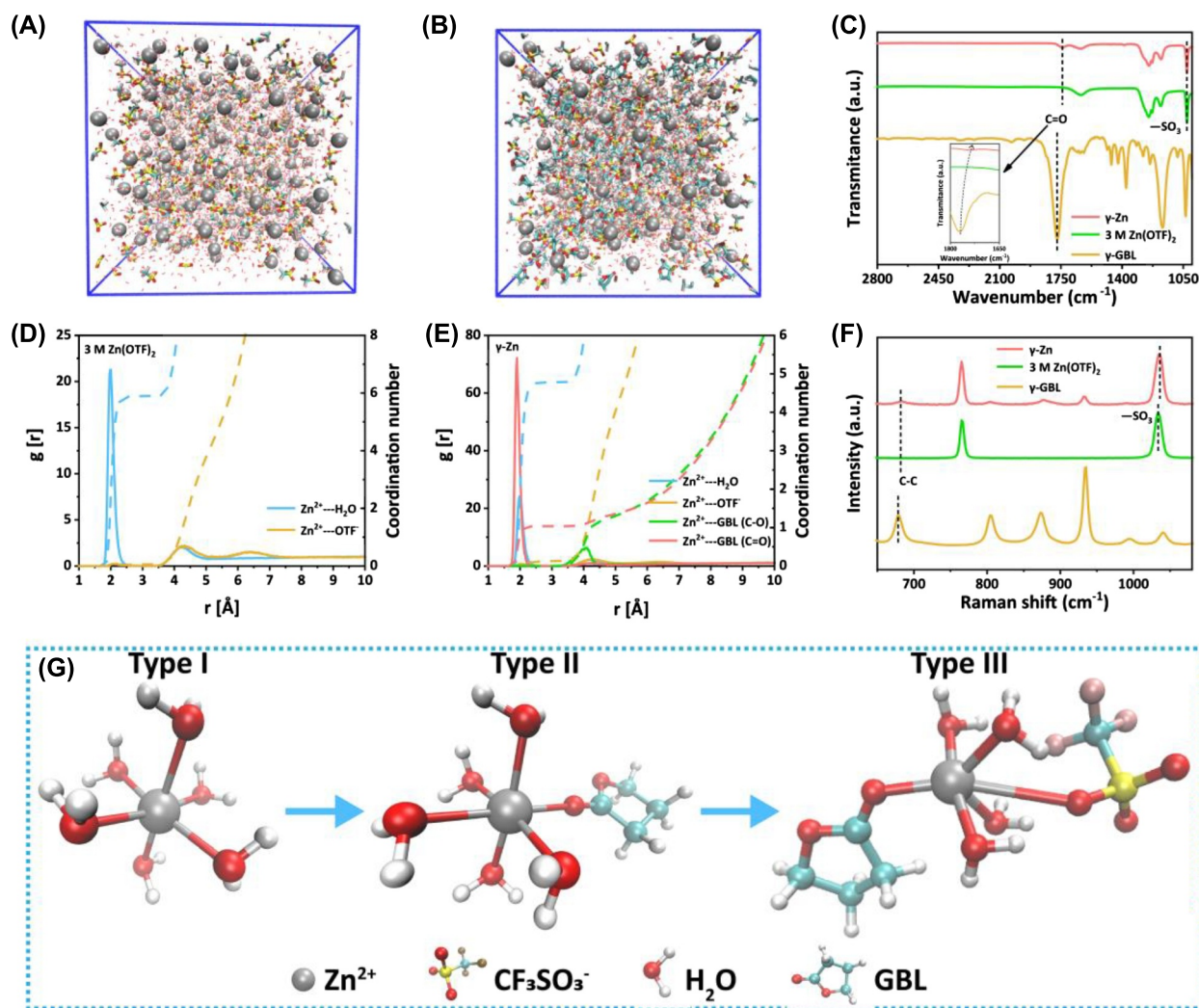
FIGURE 2 The snapshots of molecular dynamics simulation cell and the corresponding radial distribution function (RDF) plots for (A, D) 3 M Zn(OTF)$_2$ and (B, E) γ-Zn. (C) Fourier transform infrared and (F) Raman spectra of γ-GBL, 3 M Zn(OTF)$_2$, and γ-Zn. (G) Different types of Zn^{2+}-solvation structures in 3 M Zn(OTF)$_2$ and γ-Zn.

0.2 and 0.4 V, resulting in a steadier voltage output for p-MoSe$_2$ in γ-Zn. Moreover, p-MoSe$_2$ electrode displays a higher rate performance and flatter discharge plateaus at various current densities (Figures S7 and S8). When back to the low current density of 0.2 A g^{-1} (Figure 3C, Figures S9 and S10), p-MoSe$_2$ delivers higher capacity and more stable cycling performance without obvious capacity decay for 500 cycles in γ-Zn.

In light of these better electrochemical performance, the interfacial Zn^{2+} ions transfer process of p-MoSe$_2$ electrode was explored via a series of electrochemical measurements. In Figure S11, the smaller semi-circle in the electrochemical impedance spectroscopy at 30°C represents the lower interfacial charge transfer resistance for p-MoSe$_2$ electrode in γ-Zn. Actually, the charge-transfer kinetics is influenced by the interfacial desolvation process. According to the Arrhenius equation (Figure 3D, Figure S12, and S13),[28] the calculated activation energy of interfacial

Zn^{2+} transfer for p-MoSe$_2$ electrode in γ-Zn (44.1 kJ mol^{-1}) is lower than that in 3 M Zn(OTF)$_2$ (48.8 kJ mol^{-1}), suggesting the optimized solvation shell contributes to the facile desolvation kinetics. Besides, different Zn^{2+} ions diffusion rates of p-MoSe$_2$ electrode in 3 M Zn(OTF)$_2$ and γ-Zn are compared through the relationship (Equations (1) and (2)) between the real part of impedance and low frequencies in electrochemical impedance spectroscopy, where ω, A, n, F, C, R, and T stand for the angular frequency, electrode area, reactive electron number per chemical formula, Faraday's constant, molar concentration of Zn^{2+} ions, gas constant, and testing temperature, respectively.

$$Z' = R_S + R_f + R_{ct} + \sigma_w \omega^{-0.5} \tag{1}$$

$$D_{Li^+} = R^2 T^2 / 2A^2 n^4 F^4 C^2 \sigma_w^2 \tag{2}$$
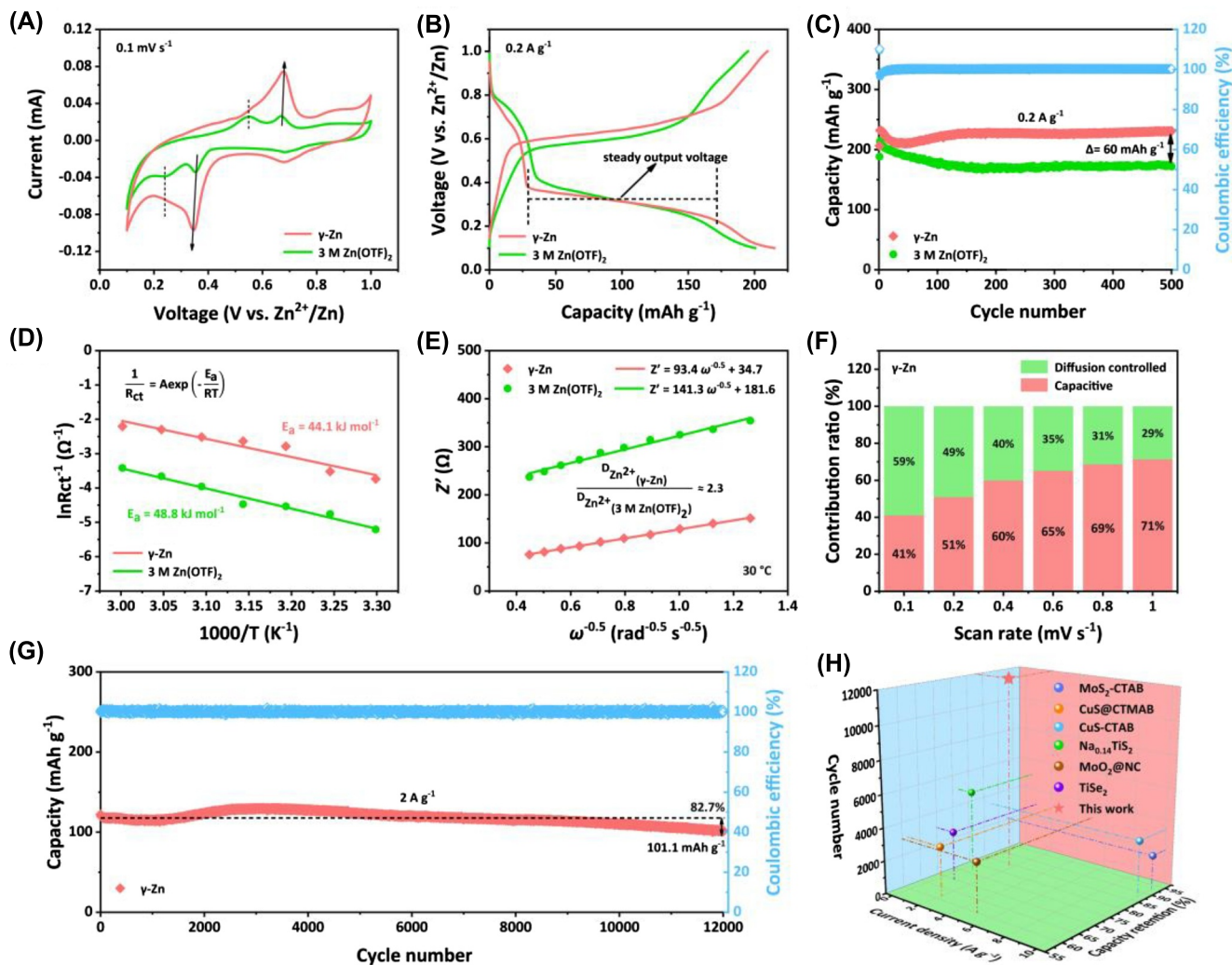
FIGURE 3 (A) CV curves of p-MoSe$_2$ electrode at 0.1 mV s^{-1} between 0.1 and 1 V (vs. Zn^{2+}/Zn) in 3 M Zn(OTF)$_2$ and γ-Zn. (B) Discharge–charge profiles of p-MoSe$_2$ at 0.2 A g^{-1} in 3 M Zn(OTF)$_2$ and γ-Zn. (C) Cycling performances of p-MoSe$_2$ electrode at 0.2 A g^{-1} in 3 M Zn(OTF)$_2$ and γ-Zn. (D) The interfacial desolvation energy barriers of p-MoSe$_2$ electrode in 3 M Zn(OTF)$_2$ and γ-Zn. (E) The difference of Zn^{2+} ions diffusion rate for p-MoSe$_2$ electrode in 3 M Zn(OTF)$_2$ and γ-Zn. (F) Capacitive contribution ratio of p-MoSe$_2$ electrode in γ-Zn. (G) Long-term cycling performance of p-MoSe$_2$ electrode at 2 A g^{-1} in γ-Zn. (H) Cycling stability of p-MoSe$_2$ electrode compared with those of previously reported superlattice electrodes and anodes for aqueous zinc-ion batteries.

As shown in Figure 3E, the Zn^{2+} diffusion rates of p-MoSe$_2$ in γ-Zn is about 2.3 times higher than that in 3 M Zn(OTF)$_2$, which is consistent with the enhanced diffusion controlled behavior in Figure 3F and Figure S14–S16. These improvements of interfacial charge transfer and bulk Zn^{2+} diffusion should further promote p-MoSe$_2$ electrode to show favorable cycling stability in γ-Zn. Surprisingly, p-MoSe$_2$ exhibits ultra-long cycling lifespan for 12,000 and 5000 cycles at 2 and 0.5 A g^{-1}, respectively (Figure 3G, Figure S17, and Figure S18). Apparently, the overall electrochemical performances of p-MoSe$_2$ have exceeded many reported superlattice materials and anodes in AZIBs (Figure 3H and Table S1),[16,17,31–34] illustrating that the strategy of regulating Zn^{2+} coordination structure in electrolyte can stabilize the layered superlattice p-MoSe$_2$ effectively.

More deeply, density functional theory calculations were carried out to analyze the Zn^{2+} intercalation behaviors of p-MoSe$_2$ electrode in γ-Zn. When a single Zn^{2+} ion is intercalating into MoSe$_2$ (Figure 4A), charge accumulation between Zn^{2+} and Se atom is almost filling to the full interlayer space. On the contrary, due to the enlarged interlayer distance, all the binding forces between Zn^{2+} and the atomic layer of p-MoSe$_2$ vanish visibly (Figure 4B), explaining the inherent characteristic that the periodically stacked superstructure benefits by weakening the electrostatic interaction between Zn^{2+} and the crystalline skeleton of superlattice. Specially, the PVP molecule can alleviate a part of the charge accumulation around Zn spontaneously, favoring the fast Zn^{2+} diffusion in the p-MoSe$_2$ layer. As a result, Zn^{2+} ions diffuse quickly with a negligible barrier of
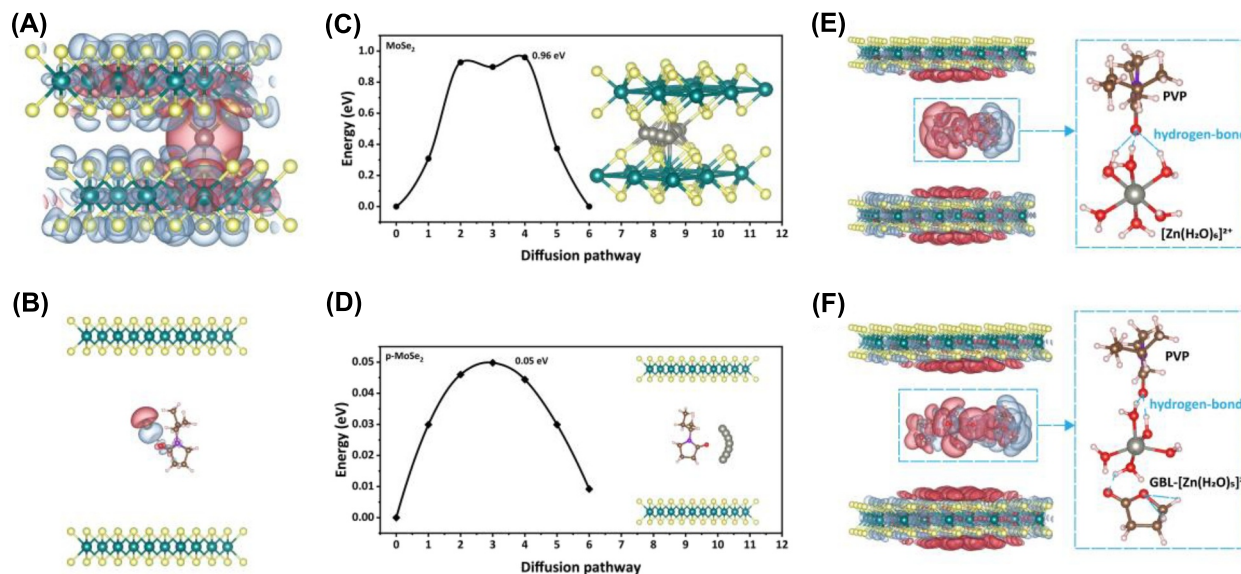
FIGURE 4 The differential charge density with Zn^{2+} intercalation in (A) $MoSe_2$ and (B) p-$MoSe_2$. Zn^{2+} diffusion pathway in (C) $MoSe_2$ and (D) p-$MoSe_2$. Differential charge density with (E) $[Zn(H_2O)_6]^{2+}$ and (F) GBL-$[Zn(H_2O)_5]^{2+}$ intercalation in p-$MoSe_2$. The red and light blue colors represent charge accumulation and depletion, respectively.

0.05 eV near the O atom of PVP (Figure 4D), while the sluggish Zn^{2+} diffusion behavior occurs in the layer structure of $MoSe_2$ because of the high barrier of 0.96 eV (Figure 4C). Furthermore, the initial intercalation states of different solvated Zn^{2+} ions in the layer p-$MoSe_2$ were also simulated. From the Figure 4E,F, it can be seen that the Zn^{2+} will interact with the interlayered PVP molecules and the solvated water will also form a hydrogen bond with the O atom of PVP, which would restrict the Zn^{2+} diffusion in the layer structure. Luckily, the strong interaction force between γ-GBL and the solvated water molecule will interrupt the hydrogen-bonded network formed by water and PVP, promoting low-resistance Zn^{2+} diffusion and high-rate performance of the p-$MoSe_2$ electrode. Besides, the charge distribution around Zn is regulated to be more symmetrical (Figure 4F), contributing to stabilizing the crystalline framework of p-$MoSe_2$ superlattice in γ-Zn. Therefore, the electrochemical reversibility of p-$MoSe_2$ in γ-Zn can be maintained as demonstrated in Figure S19 and the dynamic variations of intensity ratios of A_{1g}/E_{2g}^1 at the initial three cycles present the reliable cycling stability of p-$MoSe_2$ in γ-Zn.

From the above results, the suitable Zn^{2+}-intercalation voltage of ≈0.3–0.4 V, high-rate capability, and stable cycling performance enable p-$MoSe_2$ superlattice electrode to become an ideal anode for constructing Zn-metal free rocking chair batteries in γ-Zn. Currently, many research studies have demonstrated that the polyanion type $Na_3V_2(PO_4)_2O_2F$ (NVPF) electrode is a Zn^{2+} host to store Zn^{2+} ions at high voltage reversibly.[32] In Figure 5A, through the typical charge–discharge profiles of NVPF cathode and p-$MoSe_2$

anode, the output voltage of p-$MoSe_2$‖Zn_xNVPF rocking chair cell can be estimated at around 0.8 V, which reaches the general level of most of the Zn metal batteries (Zn‖V-O systems).[35–37] Based on the total mass of cathode and anode, the capacities of 84.8, 62.1, 43.5, 37.3, 35.5, and 28.1 mAh g^{-1} are displayed at 40, 60, 100, 160, 200, and 400 mA g^{-1}, respectively (Figure 5B,C), corresponding to the maximum energy density of 68 Wh kg^{-1}. Then, a subsequent reversible capacity of 46.7 mAh g^{-1} with a high capacity retention of 80.1% after 600 cycles at 40 mA g^{-1} (Figure S20) and the stable long-term cycling performance within 5000 cycles at 200 mA g^{-1} (Figure 5D) are also delivered, indicating the outstanding rate performance of p-$MoSe_2$‖Zn_xNVPF full cell. Furthermore, the low-temperature performance of p-$MoSe_2$‖Zn_xNVPF was also evaluated. At −40°C, p-$MoSe_2$‖Zn_xNVPF shows 38.7 mAh g^{-1} with negligible capacity decay for 320 cycles at 10 mA g^{-1} (Figure 5F). This strong low-temperature tolerance has surpassed lots of Zn metal batteries (Figure 5G), such as VO@rGO‖Zn,[38] NVP‖Zn,[39] PSC-A600‖Zn,[40] NVO‖Zn,[41] MgVO‖Zn,[42] $K_{0.5}V_2O_5$‖Zn,[43] and MNO‖Zn.[44] Besides, taking advantage of high volumetric energy density,[45–49] the attractive I_2 cathode was also selected to match with p-$MoSe_2$ anode (Figure S21). As a result, the flat plateaus during charging and discharging processes of p-$MoSe_2$ anode and I_2 cathode render p-$MoSe_2$‖ZnI_2 to display a practical output voltage of ≈ 0.5–0.6 V (Figure S22) and a maximum energy density of 56 Wh kg^{-1} (Figure S23). When the current density is adjusted to 15 mA g^{-1}, p-$MoSe_2$‖ZnI_2 displays an initial capacity of 64.7 mAh g^{-1} and a capacity retention of 71.9% after 160 cycles (Figure 5E). Obviously, the advanced
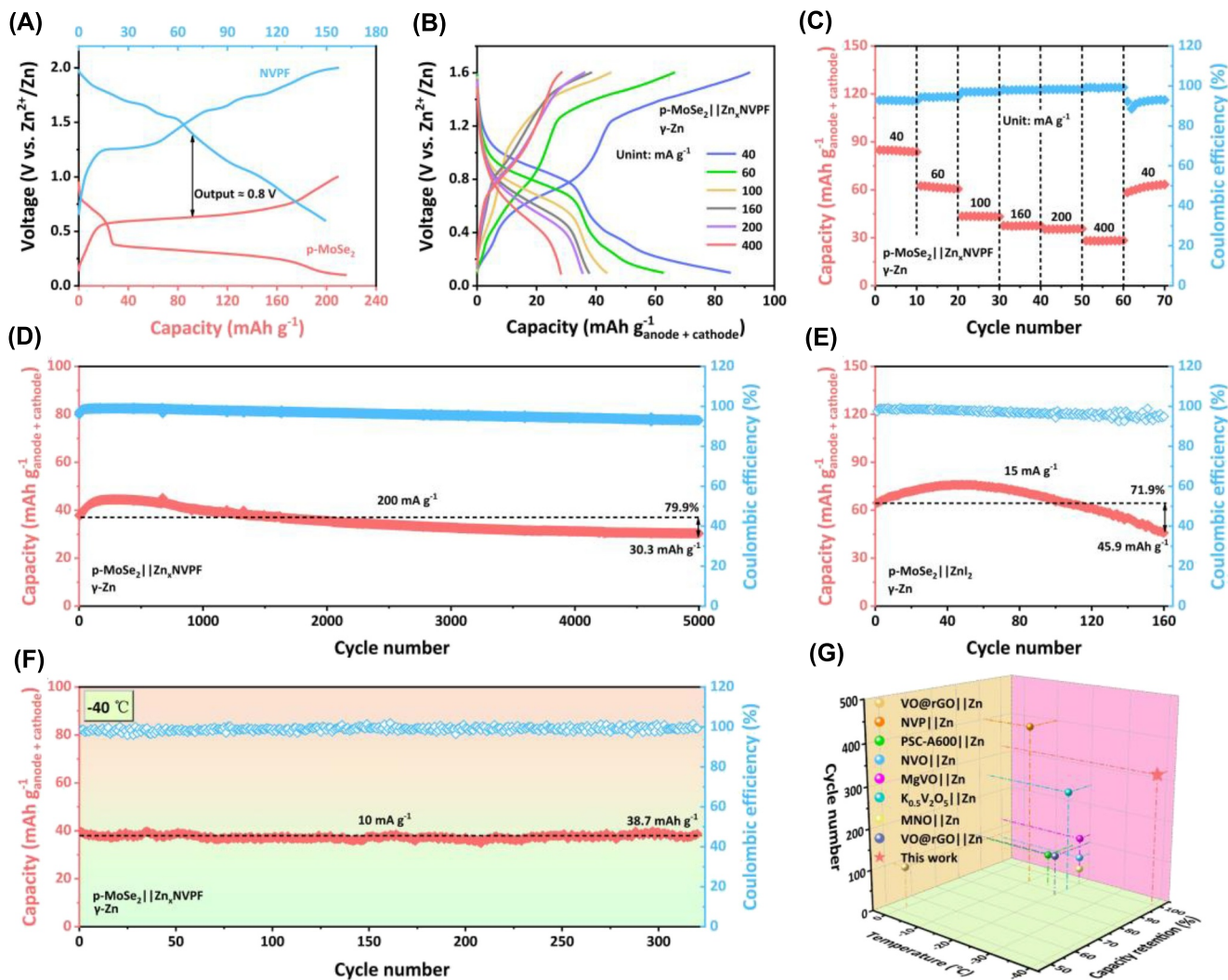
FIGURE 5 (A) The typical charge–discharge profiles of p-MoSe₂ anode and NVPF cathode. (B, C) Rate performance of p-MoSe₂||ZnₓNVPF full battery. Cycling performance of (D) p-MoSe₂||ZnₓNVPF at 200 mA g⁻¹ and (E) p-MoSe₂||ZnI₂ at 15 mA g⁻¹. (F) Cycling stability of p-MoSe₂||ZnₓNVPF at −40°C. (G) Low-temperature tolerance of p-MoSe₂||ZnₓNVPF full cell compared with those of previously reported Zn metal batteries.

superlattice p-MoSe₂ anode possesses large potential to replace Zn metal for constructing rocking chair batteries, contributing to improving the cycling stability and Zn utilization of AZIBs.

3 | CONCLUSION

In general, the superlattice p-MoSe₂ derived from intercalating organic PVP long-chain molecules into the interlayer structure of MoSe₂ is synthesized successfully. The merits of ultra-large interlayer space and enhanced electronic conductivity enable p-MoSe₂ to exhibit a flat discharge plateau at ≈ 0.3–0.4 V. After introducing γ-GBL into 3 M Zn(OTF)₂, p-MoSe₂ shows higher capacity, steadier voltage output, and enhanced cycling stability in γ-Zn due to the optimized Zn²⁺ solvation environment with γ-

GBL participation. The changed solvated Zn²⁺ structure in γ-Zn improves the electrochemical kinetics and helps to preserve the superlattice integrity of p-MoSe₂, thereby promoting successful fabrications of high-energy p-MoSe₂||ZnI₂ and long-term cycling stable p-MoSe₂||ZnₓNVPF rocking chair full batteries. Importantly, the p-MoSe₂||ZnₓNVPF full cell can even exhibit strong low-temperature tolerance at −40°C. Hence, the means of simultaneously manipulating the solvation structure in electrolyte and the superlattice structure of electrode could provide a way to develop robust rechargeable AZIBs.

AUTHOR CONTRIBUTIONS
Zeheng Lv: Conceptualization; methodology; software; investigation; writing - original draft. **Yuanhong Kang**: Software; validation; investigation; data curation; visualization. **Rong Tang**: Software. **Jin Yang**:

Investigation. **Guanhong Chen**: Investigation. **Yuhan Hu**: Investigation. **Pengxiang Lin**: Investigation; validation. **Huiya Yang**: Investigation. **Qilong Wu**: Investigation. **Minghao Zhang**: Investigation. **Fenghua Chen**: Software; validation. **Yueying Peng**: Software; validation. **Yang Yang**: Conceptualization; writing – review and editing; supervision. **Jinbao Zhao**: Writing – review and editing; supervision.

ACKNOWLEDGMENTS

CONFLICT OF INTEREST STATEMENT
The authors declare no conflict of interest.

DATA AVAILABILITY STATEMENT
The data that support the findings of this study are available from the corresponding author upon reasonable request.

ORCID
Yang Yang https://orcid.org/0000-0003-4215-5767

REFERENCES
1. Tang B, Shan L, Liang S, Zhou J. Issues and opportunities facing aqueous zinc-ion batteries. *Energy Environ Sci.* 2019;12(11): 3288-3304. https://doi.org/10.1039/c9ee02526j

2. Song M, Tan H, Chao D, Fan HJ. Recent advances in Zn-ion batteries. *Adv Funct Mater.* 2018;28(41):1802564. https://doi.org/10.1002/adfm.201802564

3. Ding J, Gao H, Ji D, Zhao K, Wang S, Cheng F. Vanadium-based cathodes for aqueous zinc-ion batteries: from crystal structures, diffusion channels to storage mechanisms. *J Mater Chem.* 2021;9:5258-5275. https://doi.org/10.1039/d0ta10336e

4. Chen X, Ruan P, Wu X, Liang S, Zhou J. Crystal structures, reaction mechanisms, and optimization strategies of MnO_2 cathode for aqueous rechargeable zinc batteries. *Acta Phys Chim Sin.* 2021;0:2111003-2111000. https://doi.org/10.3866/pku.whxb202111003

5. Ling F, Wang L, Liu F, et al. Multi-scale structure engineering of $ZnSnO_3$ for ultra-long-life aqueous zinc-metal batteries. *Adv Mater.* 2023;35(23):2208764. https://doi.org/10.1002/adma.202208764

6. Ma L, Li Q, Ying Y, et al. Toward practical high-areal-capacity aqueous zinc-metal batteries: quantifying hydrogen evolution and a solid-ion conductor for stable zinc anodes. *Adv Mater.* 2021;33(12):2007406. https://doi.org/10.1002/adma.202007406

7. Wang L, Wang Z, Li H, et al. Aminosilane molecular layer enables successive capture-diffusion-deposition of ions toward reversible zinc electrochemistry. *ACS Nano.* 2023;17(1): 668-677. https://doi.org/10.1021/acsnano.2c09977

8. Hao J, Li B, Li X, et al. An in-depth study of Zn metal surface chemistry for advanced aqueous Zn-ion batteries. *Adv Mater.* 2020;32(34):2003021. https://doi.org/10.1002/adma.202003021

9. Cao L, Li D, Hu E, et al. Solvation structure design for aqueous Zn metal batteries. *J Am Chem Soc.* 2020;142(51):21404-21409. https://doi.org/10.1021/jacs.0c09794

10. Song Y, Ruan P, Mao C, et al. Metal–organic frameworks functionalized separators for robust aqueous zinc-ion batteries. *Nano-Micro Lett.* 2022;14(1):218. https://doi.org/10.1007/s40820-022-00960-z

11. Li C, Xie X, Liu H, et al. Integrated 'all-in-one' strategy to stabilize zinc anodes for high-performance zinc-ion batteries *Natl Sci Rev.* 2022;9:nwab177. https://doi.org/10.1093/nsr/nwab177

12. Liang H, Cao Z, Ming F, et al. Aqueous zinc-ion storage in MoS_2 by tuning the intercalation energy. *Nano Lett.* 2019;19(5): 3199-3206. https://doi.org/10.1021/acs.nanolett.9b00697

13. Xu W, Sun C, Zhao K, et al. Defect engineering activating (Boosting) zinc storage capacity of MoS_2. *Energy Storage Mater.* 2019;16:527-534. https://doi.org/10.1016/j.ensm.2018.09.009

14. Li C, Liu C, Wang Y, Lu Y, Zhu L, Sun T. Drastically-enlarged interlayer-spacing MoS_2 nanocages by inserted carbon motifs as high performance cathodes for aqueous zinc-ion batteries. *Energy Storage Mater.* 2022;49:144-152. https://doi.org/10.1016/j.ensm.2022.03.048

15. Li S, Liu Y, Zhao X, et al. Sandwich-like heterostructures of MoS_2/graphene with enlarged interlayer spacing and enhanced hydrophilicity as high-performance cathodes for aqueous zinc-ion batteries. *Adv Mater.* 2021;33(12):2007480. https://doi.org/10.1002/adma.202007480

16. Yao Z, Zhang W, Ren X, et al. A volume self-regulation MoS_2 superstructure cathode for stable and high mass-loaded Zn-ion storage. *ACS Nano.* 2022;16(8):12095-12106. https://doi.org/10.1021/acsnano.2c02330

17. Zhang J, Lei Q, Ren Z, et al. A superlattice-stabilized layered CuS anode for high-performance aqueous zinc-ion batteries. *ACS Nano.* 2021;15(11):17748-17756. https://doi.org/10.1021/acsnano.1c05725

18. Zhang C, Fei B, Yang D, et al. Robust lithium–sulfur batteries enabled by highly conductive WSe_2-based superlattices with tunable interlayer space. *Adv Funct Mater.* 2022;32(24): 2201322. https://doi.org/10.1002/adfm.202201322

19. Wang H, Lu Z, Xu S, et al. Electrochemical tuning of vertically aligned MoS_2 nanofilms and its application in improving hydrogen evolution reaction. *Proc Natl Acad Sci USA.* 2013; 110(49):19701-19706. https://doi.org/10.1073/pnas.1316792110

20. Li C, Ge W, Qi S, et al. Manipulating electrocatalytic polysulfide redox kinetics by 1D core–shell like composite for lithium–sulfur batteries. *Adv Energy Mater.* 2022;12(16):2103915. https://doi.org/10.1002/aenm.202103915

21. Li Y, Dong X, Xu Z, et al. Piezoelectric 1T phase $MoSe_2$ nanoflowers and crystallographically textured electrodes for enhanced low-temperature zinc-ion storage. *Adv Mater.* 2023; 35(6):2208615. https://doi.org/10.1002/adma.202208615

22. Zhao X, Liu Q, Zhong C, et al. Activated proton storage in molybdenum selenide through electronegativity regulation. *Adv Funct Mater.* 2022;32(43):2205874. https://doi.org/10.1002/adfm.202205874

23. Li N, Zhou Q, Lin J, Lu Y, Hou Z, Qian Y. One-pot synthesis of uniform $MoSe_2$ nanoparticles as high performance anode materials for lithium/sodium ion batteries. *J Alloys Compd.* 2022;922:166306. https://doi.org/10.1016/j.jallcom.2022.166306

24. Zhou L, Yang C, Zhu W, et al. Boosting alkaline hydrogen evolution reaction via an unexpected dynamic evolution of

molybdenum and selenium on $MoSe_2$ electrode. *Adv Energy Mater*. 2022;12(47):2202367. https://doi.org/10.1002/aenm.202202367

25. Xiao P, Wu Y, Fu J, et al. Enabling high-rate and high-areal-capacity Zn deposition via an interfacial preferentially adsorbed molecular layer. *ACS Energy Lett*. 2023;8(1):31-39. https://doi.org/10.1021/acsenergylett.2c02339

26. Qiu M, Jia H, Lan C, Liu H, Fu S. An enhanced kinetics and ultra-stable zinc electrode by functionalized boron nitride intermediate layer engineering. *Energy Storage Mater*. 2022;45:1175-1182. https://doi.org/10.1016/j.ensm.2021.11.018

27. Zhao Z, Wang R, Peng C, et al. Horizontally arranged zinc platelet electrodeposits modulated by fluorinated covalent organic framework film for high-rate and durable aqueous zinc ion batteries. *Nat Commun*. 2021;12(1):6606. https://doi.org/10.1038/s41467-021-26947-9

28. Chu Y, Zhang S, Wu S, Hu Z, Cui G, Luo J. *In situ* built interphase with high interface energy and fast kinetics for high performance Zn metal anodes. *Energy Environ Sci*. 2021;14(6):3609-3620. https://doi.org/10.1039/d1ee00308a

29. Ma Q, Gao R, Liu Y, et al. Regulation of outer solvation shell toward superior low-temperature aqueous zinc-ion batteries. *Adv Mater*. 2022;34(49):2207344. https://doi.org/10.1002/adma.202207344

30. Liu DS, Zhang Y, Liu S, et al. Regulating the electrolyte solvation structure enables ultralong lifespan vanadium-based cathodes with excellent low-temperature performance. *Adv Funct Mater*. 2022;32(24):2111714. https://doi.org/10.1002/adfm.202111714

31. Lv Z, Wang B, Ye M, Zhang Y, Yang Y, Li CC. Activating the stepwise intercalation–conversion reaction of layered copper sulfide toward extremely high capacity zinc-metal-free anodes for rocking-chair zinc-ion batteries. *ACS Appl Mater Interfaces*. 2022;14(1):1126-1137. https://doi.org/10.1021/acsami.1c21168

32. Wang B, Yan J, Zhang Y, Ye M, Yang Y, Li CC. In situ carbon insertion in laminated molybdenum dioxide by interlayer engineering toward ultrastable "rocking-chair" zinc-ion batteries. *Adv Funct Mater*. 2021;31(30):2102827. https://doi.org/10.1002/adfm.202102827

33. Wen L, Wu Y, Wang S, et al. A novel $TiSe_2$ (de)intercalation type anode for aqueous zinc-based energy storage. *Nano Energy*. 2022;93:106896. https://doi.org/10.1016/j.nanoen.2021.106896

34. Li W, Wang K, Cheng S, Jiang K. An ultrastable presodiated titanium disulfide anode for aqueous "rocking-chair" zinc ion battery. *Adv Energy Mater*. 2019;9(27):1900993. https://doi.org/10.1002/aenm.201900993

35. Guo J, Ming J, Lei Y, et al. Artificial solid electrolyte interphase for suppressing surface reactions and cathode dissolution in aqueous zinc ion batteries. *ACS Energy Lett*. 2019;4(12):2776-2781. https://doi.org/10.1021/acsenergylett.9b02029

36. Lv T, Zhu G, Dong S, et al. Co-intercalation of dual charge carriers in metal-ion-confining layered vanadium oxide nanobelts for aqueous zinc-ion batteries. *Angew Chem Int Ed*. 2023;62:e202216089. https://doi.org/10.1002/anie.202216089

37. Kim Y, Park Y, Kim M, Lee J, Kim KJ, Choi JW. Corrosion as the origin of limited lifetime of vanadium oxide-based aqueous zinc ion batteries. *Nat Commun*. 2022;13(1):2371. https://doi.org/10.1038/s41467-022-29987-x

38. Huang J-Q, Lin X, Tan H, Du X, Zhang B. Realizing high-performance Zn-ion batteries by a reduced graphene oxide block layer at room and low temperatures. *J Energy Chem*. 2020;43:1-7. https://doi.org/10.1016/j.jechem.2019.07.011

39. Liu S, Lei T, Song Q, Zhu J, Zhu C. High energy, long cycle, and superior low temperature performance aqueous Na–Zn hybrid batteries enabled by a low-cost and protective interphase film-forming electrolyte. *ACS Appl Mater Interfaces*. 2022;14(9):11425-11434. https://doi.org/10.1021/acsami.1c23806

40. Li Z, Chen D, An Y, et al. Flexible and anti-freezing quasi-solid-state zinc ion hybrid supercapacitors based on pencil shavings derived porous carbon. *Energy Storage Mater*. 2020;28:307-314. https://doi.org/10.1016/j.ensm.2020.01.028

41. Chen S, Zhang Y, Geng H, Yang Y, Rui X, Li CC. Zinc ions pillared vanadate cathodes by chemical pre-intercalation towards long cycling life and low-temperature zinc ion batteries. *J Power Sources*. 2019;441:227192. https://doi.org/10.1016/j.jpowsour.2019.227192

42. Xu W, Liu C, Ren S, et al. A cellulose nanofiber–polyacrylamide hydrogel based on a co-electrolyte system for solid-state zinc ion batteries to operate at extremely cold temperatures. *J Mater Chem*. 2021;9(45):25651-25662. https://doi.org/10.1039/d1ta08023g

43. Su G, Chen S, Dong H, et al. Tuning the electronic structure of layered vanadium pentoxide by pre-intercalation of potassium ions for superior room/low-temperature aqueous zinc-ion batteries. *Nanoscale*. 2021;13(4):2399-2407. https://doi.org/10.1039/d0nr07358j

44. Geng H, Cheng M, Wang B, Yang Y, Zhang Y, Li CC. Electronic structure regulation of layered vanadium oxide via interlayer doping strategy toward superior high-rate and low-temperature zinc-ion batteries. *Adv Funct Mater*. 2020;30(6):1907684. https://doi.org/10.1002/adfm.201907684

45. Pan H, Li B, Mei D, et al. Controlling solid–liquid conversion reactions for a highly reversible aqueous zinc–iodine battery. *ACS Energy Lett*. 2017;2(12):2674-2680. https://doi.org/10.1021/acsenergylett.7b00851

46. Yang Y, Liang S, Lu B, Zhou J. Eutectic electrolyte based on *N*-methylacetamide for highly reversible zinc–iodine battery. *Energy Environ Sci*. 2022;15(3):1192-1200. https://doi.org/10.1039/d1ee03268b

47. Li Z, Wu X, Yu X, et al. Long-Life aqueous $Zn–I_2$ battery enabled by a low-cost multifunctional zeolite membrane separator. *Nano Lett*. 2022;22(6):2538-2546. https://doi.org/10.1021/acs.nanolett.2c00460

48. Yang H, Qiao Y, Chang Z, Deng H, He P, Zhou H. A metal–organic framework as a multifunctional ionic sieve membrane for long-life aqueous zinc–iodide batteries. *Adv Mater*. 2020;32(38):2004240. https://doi.org/10.1002/adma.202004240

49. Sonigara KK, Zhao J, Machhi HK, Cui G, Soni SS. Self-assembled solid-state gel catholyte combating iodide diffusion and self-discharge for a stable flexible aqueous $Zn–I_2$ battery. *Adv Energy Mater*. 2020;10(47):2001997. https://doi.org/10.1002/aenm.202001997

SUPPORTING INFORMATION

Additional supporting information can be found online in the Supporting Information section at the end of this article.

How to cite this article: Lv Z, Kang Y, Tang R, et al. Stabilizing layered superlattice $MoSe_2$ anodes by the rational solvation structure design for low-temperature aqueous zinc-ion batteries. *Electron*. 2023;1:e5. https://doi.org/10.1002/elt2.5